An airbrush 3D printer

Additive manufacturing of relaxor ferroelectric actuators

IJssel de Schepper, Stijn; Hunt, Andres

DOI
10.1016/j.addma.2024.103982

Publication date
2024

Document Version
Final published version

Published in
Additive Manufacturing

Citation (APA)
IJssel de Schepper, S., & Hunt, A. (2024). An airbrush 3D printer: Additive manufacturing of relaxor ferroelectric actuators. *Additive Manufacturing* , *81*, Article 103982. https://doi.org/10.1016/j.addma.2024.103982

Additive Manufacturing 81 (2024) 103982

Contents lists available at ScienceDirect

Additive Manufacturing

journal homepage: www.elsevier.com/locate/addma

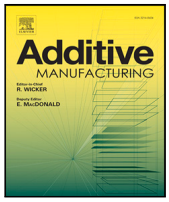

Research paper

An airbrush 3D printer: Additive manufacturing of relaxor ferroelectric actuators

Stijn IJssel de Schepper, Andres Hunt *

Department of Precision and Microsystems Engineering, Delft University of Technology, Mekelweg 2, Delft, 2628CD, Zuid-Holland, The Netherlands

ARTICLE INFO

Keywords:
Airbrush 3D printer
Spray printing
Smart material actuator
Additive manufacturing
Electroactive polymer

ABSTRACT

The additive manufacturing of electroactive polymer (EAP) devices poses significant challenges due to their distinct structure and dissimilar properties of their constituent materials. It requires deposition of multiple functional materials with different properties, achieving μm-scale resolution in layer thickness, and executing incremental deposition and curing steps while preserving the previously deposited functional material layers. This study introduces an airbrush 3D printer concept and employs it for fabricating EAP transducers. An airbrush 3D printer was constructed by adapting a standard extrusion printer platform and integrating it with a two fluid atomizer (i.e. an airbrush) as the deposition tool. A process was developed for printing of the bending P(VDF-TrFE-CTFE) actuators with carbon black electrodes, and actuators with a single and dual EAP layers were fabricated. The airbrush printer attained in-plane resolution of 0.5 mm, thickness resolutions of 0.63 μm and allowed atomizing up to 7% P(VDF-TrFE-CTFE) solutions. The 18 mm × 4 mm EAP actuators achieved 340 μm (440 V_{pp}) and 3.7 mm (400 V_{pp}, 104 Hz) tip deflections respectively in quasi-static and resonant operation. Airbrush printing therefore proved to be a robust method for printing precursor materials with a wide range of properties, and is anticipated to be a versatile approach for printing other passive and stimuli-responsive materials and devices.

1. Introduction

The unique properties of smart material transducers enable actuation and sensing in diverse scenarios where conventional transducers are lacking [1,2]. Transduction in such sensors and actuators is achieved via deformation of a functional material, making the structure inherently simple, avoiding complex mechanisms and moving components. The simple structure significantly improves their miniaturization outlooks over the conventional transducers and allows to configure them in almost any shape and geometry. Electroactive polymer (EAP) transducers can be directly controlled and read by electronic circuits, are low in stiffness and allow large deformations [2]. Compared to the conventional ceramics-based piezoelectric materials that are widely used in high-bandwidth sensing and actuation applications [3], EAPs are soft and compatible with higher material strains [1], characteristic to the polymers. Such properties facilitate various applications that are infeasible or impractical with conventional actuators, e.g. in microrobotics [4], vibration suppression [5], organ-on-chip devices [6], microfluidics [7,8] and energy harvesting [9]. Developing EAPs and EAP-based devices however requires versatile fabrication techniques that allow sub-micron resolutions in thickness direction and custom geometries of various resolutions in other dimensions.

Conventional manufacturing of the EAP transducers bases on techniques such as screen printing [10], solution casting [11] spin coating [12], doctor-blading [13] and sputter coating [14]. As a simple and accessible non-contact fabrication method, airbrushing has been employed in fabricating EAP actuators [15] and their components [16–18]. Patterning in all these methods is implemented by using masks, thus introducing the need for additional fabrication steps for each design. Creating custom designs is limited by the masking capabilities and repeatability, and becomes very labor-intensive for prototyping and small volume production. Besides masking limitations, lack of automation means higher labor intensity and compromised repeatability.

Automation via the additive manufacturing can alleviate these challenges and facilitate the integration of the smart materials into mechanical and electronic devices. Extrusion printing has been employed to print ionic EAP transducers [19,20] and electronic EAP sensor structures [21]. Direct ink writing (DIW) has been employed for fabricating dielectric elastomer actuators [22,23] and depositing PVDF-based EAPs [24]. Thickness resolution in these methods (tens of μm) is sufficient for piezoelectric sensors (thicker layers yield stronger signals) and ionic EAP transducers (ions can migrate through the thick EAP).

* Corresponding author.
E-mail address: a.hunt@tudelft.nl (A. Hunt).

https://doi.org/10.1016/j.addma.2024.103982
Received 21 July 2023; Received in revised form 29 December 2023; Accepted 12 January 2024
Available online 13 January 2024

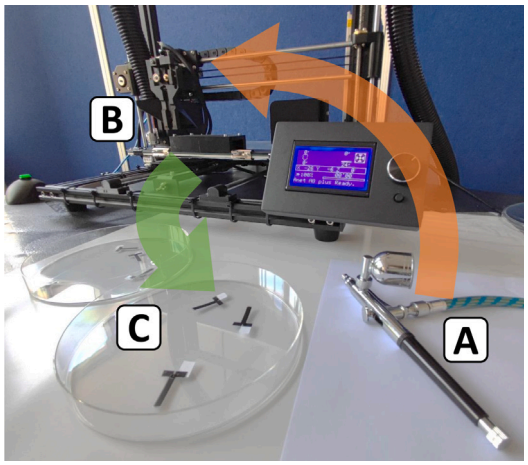

Fig. 1. The proposed concept: introducing an airbrush tool (A) into a 3D printer (B) for spray printing smart material transducers (C).

For electronic EAP actuators, finer layer resolution and quality are needed in order to attain sub-kV operating voltages and prevent dielectric breakdown, requiring non-contact manufacturing methods. Electrohydrodynamic deposition (EHD) has been reported to print 91 nm thick piezoceramic films [25], and could be also employed for EAP transducer manufacture. Manufacturing EAP devices by inkjet printing (IJP) [26] and aerosol jet printing (AJP) [27] allows sub-micron layer thicknesses and down to 10 μm in-plane resolutions [28]. Inkjet printing is limited by a narrow range of ink rheological properties and suspended particle sizes that are feasible to print [26], requiring hours to deposit dissolved EAPs and causing nozzle clogging [29–32]. While AJP allows printing up to 2500 cP viscosities [27,33], viability of AJP, IJP and EHD methods is limited by the complexity and cost of the equipment and low deposition rate (i.e. serial processes).

This paper proposes an automated spray-deposition concept for fabricating smart material sensors and actuators basing on a fine resolution airbrush. The proposed approach is significantly less complex than the AJP, IJP and EHD methods, aiming to combine the benefits of: (1) contact-less methods, allowing sub-micron films thicknesses; (2) mask-less methods, capable of arbitrary patterns at sub-mm in-plane resolutions; and (3) automated process, improving repeatability and reducing labor-intensity. The spray printer concept is proposed and built basing on a consumer-grade 3D printer and a high-resolution two fluid atomizer (i.e. an aibrush), as described in Section 2.1 and illustrated in Fig. 1. Actuator fabrication focuses on a bending unimorph transducer design that consists of the P(VDF-TrFE-CTFE) polymer (i.e. a relaxor ferroelectric EAP) and carbon black electrodes, as explained in Section 2.2. The best printing resolutions for depositing these materials in the spray printer are studied according to Section 2.3, and the parameters for printing each component of the actuators are developed according to Section 2.4. Next, the actuators are manufactured and characterized, respectively following the steps described in Sections 2.5 and 2.6. The results of the spray printing resolution study, actuator fabrication and performance characterization are presented in Section 3 and discussed in Section 4. This paper is concluded in Section 5.

2. Materials and methods

2.1. An airbrush 3D printer

The 3D printer for spray deposition of the EAP transducers was constructed from a two-fluid atomizer, a 3D printer platform, an air source and a fume extractor. A schematic representation of the system components and their interconnection is given in Fig. 2.

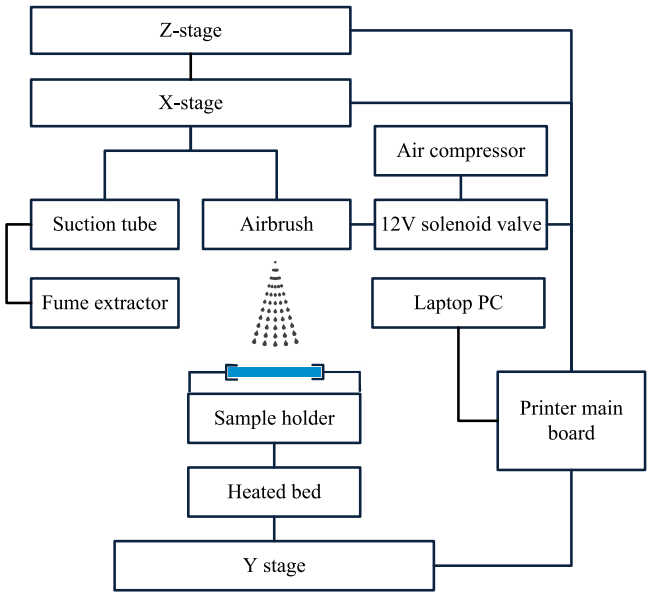

Fig. 2. The principle construction of the spray printer.

Airbrush selection defines the spray properties, i.e. the shape, pattern and droplet size characteristics [34]. For this study a two fluid atomizer Iwata Custom Micron Takumi (Anest Iwata-Medea Inc) was chosen [35]. It is a side-feed dual-action airbrush with a 0.18 mm nozzle, capable of depositing very fine lines (ca 0.18 mm to 20 mm). Better resolutions than 0.18 mm (i.e. the nozzle diameter) are not anticipated since the airbrush does not use aerodynamic focusing, making the spray envelope of the atomized ink divergent. The minimum working distance is limited by the needle that controls the ink feed rate and protrudes from the nozzle.

An Anet A8 Plus 3D printer was chosen as the donor platform for building the spray printer. It is a simple and affordable system with a large build volume (300 mm by 300 mm by 350 mm) to accommodate all the required modifications. The system allows a 12 μm positioning accuracy in the x and y directions, and 4 μm in the z direction. These are well sufficient capabilities, given that the spray deposition is not anticipated to attain better in-plane resolution than the nozzle diameter (i.e. 0.18 mm).

A dedicated airbrush tool assembly is designed to (1) mount the airbrush, (2) control its needle valve position, (3) provide the compressed air input, and (4) remove the exhaust gases, as explained in the following. (1) The x-carriage of the printer was redesigned to hold the airbrush vertically over the printing bed. It was made of 3D-printed PLA (Prusa i3 MK3) and replaced the original filament extruder assembly of the Anet A8 Plus x-carriage; (2) The rear casing of the airbrush was removed to expose the flow control needle. The needle was connected via a rack and pinion drive to the re-purposed extruder motor, allowing to control the liquid flow rate via the 3D printer instructions file (GCODE); (3) The air supply port of the airbrush was connected via a flexible tube to a compressor (AG-326, Airgoo). The air line was passed via a pneumatic on-off valve, allowing to toggle the air supply from the printer control signal; and (4) To extract the excess spray and gases from the proximity of the printing site, an extraction mouthpiece was designed and integrated with the printer x-carriage. This allowed to attach a flexible tube, that was further connected to a fume extractor (BVX-200, Metcal).

A sample holder was designed to allow easy loading of the printing substrates onto the printbed, and spring-loaded clamps were used to hold them in place. Printing instructions were sent from a PC computer to the modified printer using the Printrun 2.0.0 software and a USB interface.

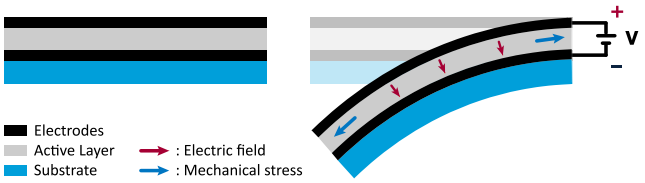

Fig. 3. Working principle of a unimorph bending actuator.

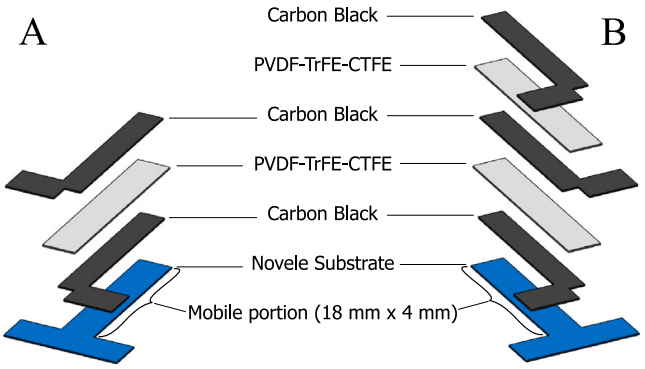

Fig. 4. Actuator morphology: A – the single layer design; and B – the dual layer design.

2.2. EAP actuators

This study investigates printing of the bending unimorph cantilever actuators basing on the P(VDF-TrFE-CTFE) polymer for the EAP and carbon black for the electrodes. Principle of operation of such actuators is explained in Fig. 3, showing how the active layer contracts under the electric field, causing a bending moment and a subsequent deflection along the beam. Actuator designs and materials are explained in the following.

2.2.1. Designs

Two realizations of the unimorph actuator design are considered. The first design bases on a single film of EAP in the active layer. It consists of a total of four layers of material, as illustrated in Fig. 4A: a flexible substrate, the bottom electrode, an EAP layer, and the top electrode. The electrodes are necessary to apply an electric field across the EAP thickness. The second design bases on two films of EAP within the active layer. It consists of a total of six layers of material, as illustrated in Fig. 4B – in addition to the single layer design it contains another layer of EAP and electrode.

Actuator designs are T-shaped, consisting of a wider passive base and an active cantilever portion that protrudes from the base. The base is used to clamp the actuator mechanically and electrically, separating the opposite polarity contact pads to the opposite sides. Dimensions of the actuator portion are 18 mm by 4 mm, and there is a 0.5 mm offset left between the active area and the edge of the sample, preventing short-circuiting of the electrodes at the sample boundaries.

2.2.2. Materials

All actuator designs (Fig. 4) are constructed from three materials (Figs. 3 and 4), serving as the flexible substrate, conductive electrodes and electroactive polymer layers. The choice and rationale for the respective materials is as follows: (1) A 140 μm thick PET substrate with a microporous resin coating (Novele IJ-220, Novacentrix) was chosen for the substrate material. It serves as the passive layer in the actuator design (Fig. 3), and all other layers are printed on it. The ink deposited on this substrate does not spread as easily as on the non-porous substrates (e.g. polyimide), allowing to deposit finer feature sizes, near the airbrush atomizer's capabilities limits; (2) A carbon black nanoparticle dispersion ink with a 5 wt% loading factor (JR700-HV, Novacentrix) was chosen for the conductive electrodes. This ink becomes conductive after solvent evaporation without additional post-processing, and its conductivity is well sufficient for the low-capacitance relaxor ferroelectric actuators [36]. Due to its relatively large particle sizes it does not pose significant health concerns [37]. Alternatively, metal nanoparticle inks could be used, introducing the need for additional thermal or photonic processing and requiring additional attention to the health risks [38,39]. Carbon black inks are also more affordable than the metal nanoparticle inks; and (3) The active layer based on the Piezotech RT-TS poly(vinylidene fluoride-trifluoroethylene-chlorotrifluoroethylene) electroactive polymer powder from Arkema (i.e. P(VDF-TrFE-CTFE) in short). It is a relaxor ferroelectric EAP, able to produce material strains of up to 5% [40]. The P(VDF-TrFE-CTFE) powder is formulated into an EAP ink by dissolving it in a solution of dimethyl sulfoxide (DMSO, Merck) and methyl ethyl ketone (MEK, Merck). Actuator fabrication based on a 7%wt concentration of P(VDF-TrFE-CTFE) in a MEK 90:10 DMSO solution.

2.3. Printing parameters and deposition resolution

The effect of printing parameters on the deposition resolution and quality were studied to determine the system capabilities, and to later establish recipes for reliable printing of the functional inks. The four most important printing parameters were identified as the (1) ink valve position s_v; (2) printing speed v_p; (3) nozzle-substrate distance s_n; and (4) air supply pressure p_g.

Individual test lines were printed at different settings by varying only one parameter at a time, as summarized in Table 1. Width and quality of the lines were then evaluated to determine the effect of each of the printing settings. Initial settings were chosen approximately in the middle of the each parameter range (v_p = 500 mm/min, s_n = 3 mm and p_g = 30 PSI), and the next steps incrementally replaced the initial values with the best performing setting. The experiments were conducted in the following order: (1) the ink valve position was varied between 0.11 mm and 0.26 mm in 0.03 mm steps, whereas no ink flow was observed at 0.06 mm and smaller positions; (2) the air supply pressure was varied between 10 PSI and 47.5 PSI in 7.5 PSI increments, i.e. covering the full operational range of the compressor; (3) the nozzle-substrate distance was varied from 0.5 mm to 9 mm in 1.5 mm increments, whereas the clearances below 0.5 mm pose a high risk of needle-substrate collisions, and clearances above 8 mm cause the fume extraction to become insufficient; and (4) the printing speed was varied from 500 mm/min to 8000 mm/min in 1500 mm/min increments, while smaller speeds deposited too much ink and above 8000 mm/min the stepper motors started missing steps due to the infeasible accelerations.

The test lines were printed on the IJ-220 substrates (Novele) using first the JR-700-HV ink. Rheological properties of the JR700-HV ink are well suited for two-fluid atomization, while the microporous coating of the IJ-220 is specifically engineered for contactless printing, minimizing the displacement and splattering of the deposited inks. This reduces the role of the secondary effects on the deposition results, i.e. the ink smearing due to the air flow above the deposition site, and the spattering of the ink. Later, the same process was repeated for the EAP ink. The 19 mm long test lines were examined for their width and quality under a Keyence VHX-6000 optical microscope. The width of the line was defined as the continuously connected (opaque-appearing) portion of the deposited ink, including the region with voids, and excluding the region where the satellite droplets become disconnected from the body of the line.

Table 1
The sequence and settings in the development of the printing recipe to produce high-resolution lines using the carbon black ink.

Experiment	#1	#2	#3	#4
Ink valve position (mm)	0.11:0.03:0.26	0.17	0.17	0.17
Air supply pressure (PSI)	30	10:7.5:47.5	40	40
Nozzle-substrate offset (mm)	3	3	0.5:1.5:9	0.5
Printing speed (mm/min)	500	500	500	500:1500:8000

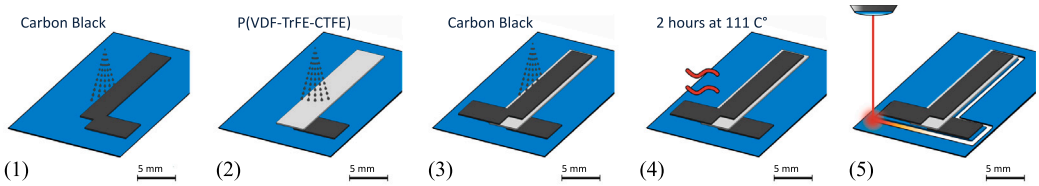

Fig. 5. Fabricating the unimorph bending actuators. Manufacturing steps for the single layer design: (1) Deposition of the bottom electrode; (2) Deposition of the active layer; (3) Deposition of the top electrode; (4) Annealing in an oven for 2 h at 111 C°; and (5) Laser cutting to separate the actuator samples from the substrate. Manufacturing of the dual layer design repeats the steps (2) to (4) one more time before separating the samples from the substrate in step (5).

2.4. Printing parameters for actuator manufacture

Spray printing at the highest resolution settings requires a very small nozzle-substrate clearance (0.5 mm), posing a high risk of collision. Relaxation of the resolution requirement to 0.7 mm allowed to increase this gap to ≥2 mm. Following the same procedure as described in Section 2.3, the printing parameters were experimentally established for depositing the lines of carbon black and EAP at the 0.7 mm resolution objective.

The recipes for printing each functional layer of the actuators (see Fig. 4) were next established under the following conditions: (1) for the bottom electrode deposition, the JR-700HV ink and IJ-220 substrate combination was used, similarly to Section 2.3; (2) for the EAP layer deposition, the P(VDF-TrFE-CTFE) ink (Section 2.2.2) and IJ-220 substrate combination was used, since the wetting properties of this substrate are similar to the carbon black electrode surface; (3) for the top electrode deposition, a combination of the JR-700HV ink and non-porous PET substrate was used, resambling the surface properties of the non-porous EAP layer. In the dual-layer actuator fabrication (Section 2.2.1) the additional layers of EAP and carbon black were deposited using the same settings as the EAP and top electrode deposition in steps (2) and (3).

2.5. Actuator manufacture

The proposed printing platform (Section 2.1) and the established deposition parameters (Section 2.4) were then used to manufacture the actuators. Fabrication of both the single- and dual-layer designs followed the steps described below and illustrated in Fig. 5.

For the bottom electrode, 4 layers of the JR700-HV ink were deposited on the IJ-220 substrate according to the recipe established in Section 2.4 (see Table 2). This results in a continuous thin film of carbon black, without any observable defects. After deposition, the bottom electrode was dried until the surface turned from glossy wet to opaque and dry in appearance. A heated airgun was used to speed up the solvent evaporation.

The EAP layer was deposited by printing the 7%wt P(VDF-TrFE-CTFE) ink (Section 2.2.2) on the bottom electrode according to the recipe established in Section 2.4 (Table 2). Completing the EAP layer required 32 printing repetitions. After every 16 repetitions the samples were allowed to dry until their appearance turned from opaque and wet to translucent and dry, indicating that most of the solvent had evaporated. Skipping this step causes a build-up of solvent droplets on top of the EAP film, that further spread across the sample in the following printing cycles.

The top electrode was printed on the EAP layer using the JR-700HV ink and following the recipe from Section 2.4 (Table 2). This differs from the bottom electrode recipe because on top of the EAP layer the ink behaves different than on the porous IJ-220 substrate. It required 16 printing repetitions to attain a uniform electrode layer. To prevent the spreading of the previously deposited layers, the samples were allowed to dry after every four repetitions until becoming matte in appearance. A heated airgun was used to speed up this process. Next, the samples were annealed in an oven for 2 h at 111 C° to remove any solvent residues and enhance the EAP semi-crystalline structure for stronger relaxor ferroelectric properties [40–42].

In case of the dual-layer actuator design (Fig. 4) the bottom electrode is deposited identically to the single-layer design, while only half the EAP thickness is deposited in the first EAP layer (i.e. 16 repetitions). The middle electrode is then deposited according to the top electrode printing recipe. Furhter, the steps of EAP deposition (again 16 print repetitions), top electrode deposition and annealing are repeated one more time (Fig. 5) to complete the actuator. Therefore, the same net amount of EAP is used in both of the actuator designs.

2.6. Actuator characterization

After fabrication the electrical isolation between the top and bottom electrode of every actuator was measured (Voltcraft VC860 multimeter) to detect any short-circuit defects. Next, the samples were experimentally characterized in both quasi-static and dynamic actuation experiments. In quasi-static analysis the voltage-deflection characteristics and actuation hysteresis were studied. In dynamic analysis the actuator frequency response was measured. An experimental set-up and the respective procedures are described in the following.

Construction of the characterization set-up is shown in Fig. 6. The T-shaped actuators were mechanically fixed by a 3D-printed clamp (PET-G, Prusa i3 MK3) with embedded silver electrodes for electrical connections. Input voltages were applied to the actuator by a high-voltage power amplifier (HVA 1500-1/50, Smart Material Inc), and the tip displacements were simultaneously measured using a laser displacement meter (ILD-1402-10, Micro-Epsilon). The experiment procedures were controlled from a NI Labview 2018 environment running on a PC computer, via a USB data acquisition card (USB-6211, National Instruments). The data was captured and stored using the same LabVIEW program, and further processed in Matlab software (R2022a).

The characterization experiments were conducted in the following sequence to prevent damage to the actuators before all necessary experiments were completed: (1) First, the actuation hysteresis experiments were conducted. A 1 Hz (bipolar) sinusoidal excitation with a 300 V amplitude was applied to the actuator and the tip deflections were simultaneously measured and stored; (2) Next, the frequency response measurements were conducted. Unipolar sinusoidal excitations with a 50 V amplitude and a 50 V offset (i.e. 100 V_{pp}) were applied at

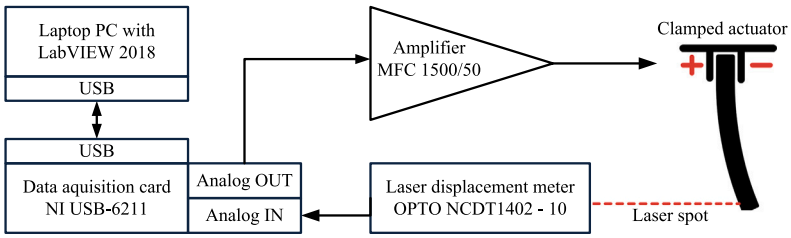

Fig. 6. Block diagram of the experimental setup for actuator characterization.

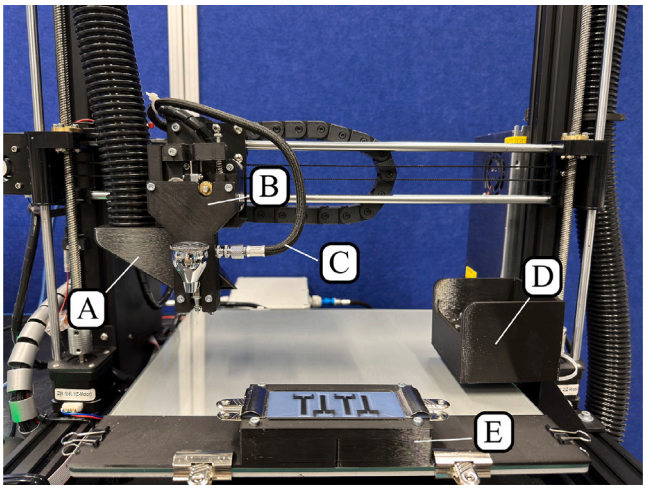

Fig. 7. The Anet A8 3D printer modified for spray printing EAP transducers. The main components of the printer are indicated as follows: A – the mouthpiece of the fume extractor; B – the printhead assembly; C – the compressed air input line; D – the purging bucket; and E – the sample holder mounted to the original printbed.

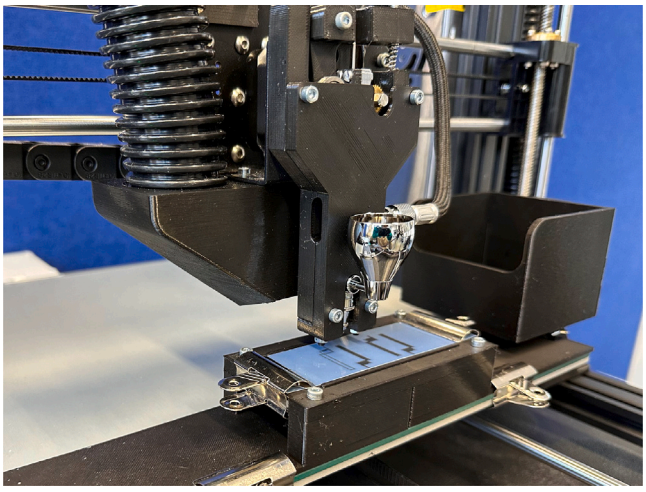

Fig. 8. Deposition of the bottom electrode. Four samples can be seen in the making, whereas only the outline has been printed for the leftmost sample. Entire fabrication process is summarized in Video 1.

600 different frequencies, logarithmically distributed between 1 Hz and 300 Hz; and (3) Finally, the voltage-deflection experiments were conducted. A 1 Hz unipolar sinusoidal excitation was applied and the amplitude was risen in 10 V increments from 0 V until the actuator broke down.

To study the actuator morphology across the thickness direction it was necessary to expose the cross-section of the samples. The actuators were cut in a femtosecond laser micromachining system (Lasea LS Lab) and imaged in a scanning electron microscope (SEM, Jeol JSM 6010LA). The surfaces profiles of the actuators, the samples from intermediate fabrication steps, and the samples of the individual printed lines were further studied using a white light interferometer (Bruker K1). Before profiling all samples were sputter-coated with a ca 20 nm thick Au layer (Jeol JFC-1300) to make them reflective.

3. Results

The proposed airbrush 3D printer was built according to Section 2.1, and the resulting system and its components are explained in Fig. 7. A close-up image of the printhead assembly during the printing process is shown in Fig. 8 and the entire fabrication process is summarized in Video 1. The following addresses the system characterization (Section 3.1), actuator fabrication (Section 3.2) and actuator performance characterization (Section 3.3) results.

3.1. System characterization

The effect of the printing settings on the line resolution and quality was studied according to Section 2.3. The experiment sequence and the incremental outcomes for the JR-700HV ink and IJ-220 substrate combination are reported in Table 1. The results are explained in the order of the experiments (see Fig. 9):

(1) Varying the ink valve position between 0.11 mm to 0.26 mm increased the line width from 1 mm to 1.7 mm, as can be seen in Fig. 9A. The ink valve positions above 0.2 mm caused the formation of additional tear-shaped droplets on the sides of the spray region that increased in size with the increasing ink flow rates. The lowest valve position that attained consistent spraying was 0.17 mm, yielding in a 1.5 mm line width.

(2) Increasing the air supply pressure from 10 PSI to 47.5 PSI produced line widths between 1.3 mm and 1.7 mm, as shown in Fig. 9B. The pressures below 17.5 PSI caused a much higher ratio of satellite droplets, deteriorating the line quality. Consistent and repeatable deposition was attained at the lowest pressure of 40 PSI.

(3) Varying the nozzle-substrate offset between 0.5 mm and 9 mm altered the line widths between 1 mm and 2.2 mm, as can be seen in Fig. 9C. The offsets below 1.5 mm produced very thin lines, but were then spread beyond the initial deposition widths by the excessive air flow. The best trade-off between these effects was observed at the 0.5 mm offset.

(4) The effect of the printing speed on the line width and quality is shown in Fig. 9D. Increasing the printing speed from 500 mm/min to 8000 mm/min decreased the line width from 1 mm to 0.5 mm. The finest continuous line widths of 0.5 mm were attained at the printing speed of 6000 mm/min.

Similar results were obtained also for the deposition of the P(VDF-TrFE-CTFE) ink. Both the JR-700HV and P(VDF-TrFE-CTFE) inks achieved a reliable deposition at the finest line widths of 0.5 mm. The respective printing settings are summarized in Table 2. For validation, a bidirectional raster scan pattern was printed using both the recipes, as shown in Fig. 10. Material distribution in the straight and turning segments of these patterns is shown in Fig. 11.

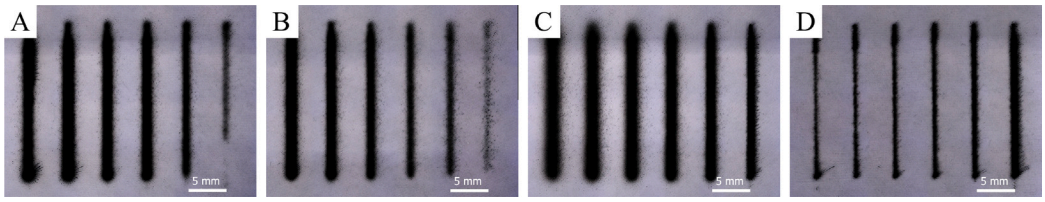

Fig. 9. The effect of the printing parameters on the line widths and quality: A – the liquid flow valve position was decreased from 0.26 mm (left) to 0.11 mm (right) in 0.03 mm increments; B – the air supply pressure was decreased from 47.5 PSI (left) to 10 PSI (right) in 7.5 PSI increments; C – the nozzle-substrate distance was decreased from 9 mm (left) to 0.5 mm (right) in 1 mm increments; and D – the printing speed was decreased from 8000 mm/min (left) to 500 mm/min (right) in 1500 mm/min increments.

Table 2
The recipe development results for printing of the fine lines and fabrication of the actuators.

Ink	Ink valve position	Air supply pressure	Nozzle-substrate offset	Printing speed	Repetitions
Printing recipes for the minimum feature sizes:					
JR-700HV	0.17 mm	40 PSI	0.5 mm	6000 mm/min	1
P(VDF TrFE-CTFE)	0.60 mm	40 PSI	0.5 mm	6000 mm/min	1
Printing recipes for actuator fabrication:					
Bottom electrode	0.17 mm	30 PSI	2.0 mm	1000 mm/min	4
Polymer layer	0.60 mm	40 PSI	3.0 mm	4000 mm/min	2 × 16
Top electrode	0.17 mm	20 PSI	4.0 mm	4000 mm/min	16

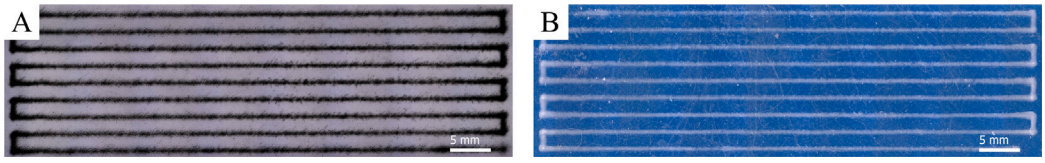

Fig. 10. Spray-printed raster patterns with a 2 mm pitch demonstrate the minimum attainable feature sizes: A – the carbon black ink; and B – the P(VDF-TrFE-CTFE) ink.

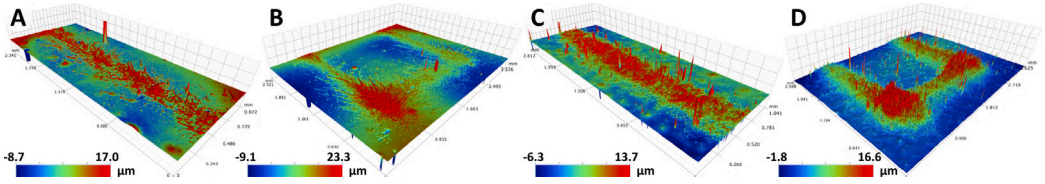

Fig. 11. White light interferometry (Bruker K1) results show material distribution in the printed raster patterns (Fig. 10). A – carbon black straight segment; B – carbon black turn; C – P(VDF-TrFE-CTFE) straight segment; and D – P(VDF-TrFE-CTFE) turn. The larger spikes are caused by dust particles that are exaggerated by the very high magnification of the vertical axis.

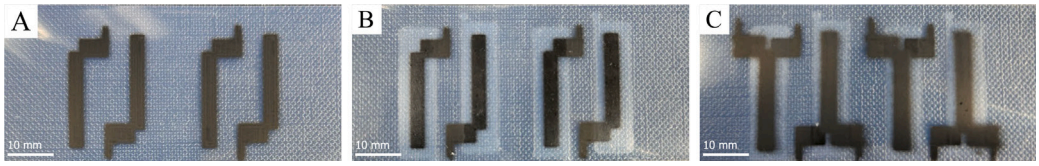

Fig. 12. The intermediate outcomes of the manufacturing process: A – the bottom electrode is deposited on the IJ-220 substrate; B – the P(VDF-TrFE-CTFE) layer is deposited on the bottom electrode; C – the top electrode is deposited on the P(VDF-TrFE-CTFE) layer.

3.2. Manufacturing results

Printing settings for the electrode and the EAP layer deposition were developed according to Section 2.4 and are summarized in Table 2. Both the single-layer and dual-layer actuator designs of Fig. 4 were manufactured according to Section 2.5. The intermediate and the final results of fabricating single-layer actuator samples are shown in Fig. 12. Material distribution in these samples is respectively visualized in Fig. 13 and profiled in Fig. 14. The cross-sections of both the single- and dual-layer actuator samples were imaged in SEM, as shown in Fig. 15. The EAP layer thickness measured ca 20 µm in the single layer samples and ca 10 µm per layer in the dual layer samples. The electrode boundaries appeared irregular in the laser-ablated interfaces and therefore could not be measured. The same settings were used to print separate electrode samples that measured 1 µm in thickness in SEM. All the single-layer actuator samples showed no measurable conductivity between the top and the bottom electrodes (i.e. resistance > 40 MΩ), indicating a good EAP layer quality. Two out of the three dual-layer samples measured a lower resistance (ca 100 kΩ), indicating the presence of very thin areas in the EAP layer.

3.3. Performance characterization

Three samples of both the single-layer and dual-layer designs were studied according to the methodology described in Section 2.6, and additional experiments were conducted on more samples to extract their maximum performance characteristics. Functionality and performance of the spray-printed actuators was first characterized in terms of

Table 3
Summary of the actuation performances and comparison against the previously reported similar actuators.

Actuator	Maximum quasi-static deflection	Maximum resonant deflection	Resonant frequency	Breakdown voltage
Actuators by Baelz et al. [29]	206 μm (300 V)	3.0 mm (300 V)	110 Hz	300 V
Actuators by Sekar [30]	224 μm (275 V)	1.7 mm (200 V)	114 Hz	275 V
Single layer actuator	179 μm (630 V)	2.0 mm (600 V)	107 Hz	560 V–630 V
Dual layer actuator	340 μm (440 V)	3.7 mm (400 V)	104 Hz	280 V–440 V

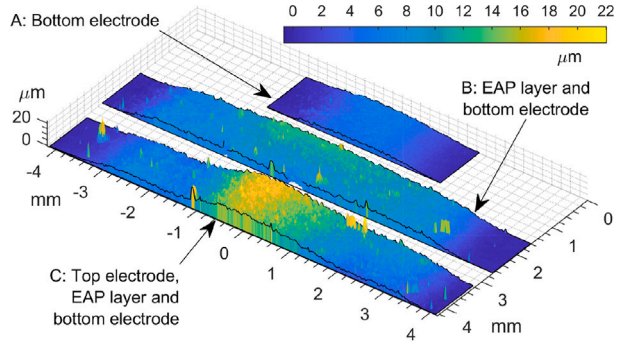

Fig. 13. Profiles of the actuator samples after each manufacturing step, showing the material distribution over the width of the samples in Fig. 12 (Bruker K1). A – the bottom electrode on the IJ-220 substrate; B – the P(VDF-TrFE-CTFE) layer deposited over the bottom electrode; and C – the top electrode deposited on the P(VDF-TrFE-CTFE) layer. Accuracy of these measurements is limited by the uniformity of the flexible polymer substrate.

their deflection-voltage relation, actuation hysteresis and frequency response. The voltage-deflection relationships for all actuators are shown in Fig. 16. In quasi-static actuation the single layer samples produced 179 μm displacements upon 630 V_{pp} excitation, and the dual layer samples respectively 340 μm upon 440 V_{pp}. Hysteresis behavior over one cycle of the sinusoidal excitation (1 Hz, 300 V) is given for both the actuator types in Fig. 17. The first resonant frequency of all the actuators remained within the 100 Hz–110 Hz interval. Frequency responses at the 100 V_{pp} excitation are plotted in Fig. 18. Applying elevated voltages at the actuator resonant frequency resulted in much larger strains – the single- and dual-layer actuators respectively produced deflections of 1.98 mm (107 Hz, 600 V_{pp} excitation) and 3.73 mm (104 Hz, 400 V_{pp} excitation). The characterization results are summarized in Table 3.

4. Discussion

4.1. Spray printing system

A novel additive manufacturing platform was proposed and developed for spray printing EAP transducers. The spray printer enables contact-less, mask-less and automated deposition of inks with a wide range of rheological properties and containing larger microparticles. It allows to print materials that are problematic to handle in other 3D printing techniques, to create complex geometries at sub-mm in-plane resolutions and sub-μm thickness resolutions. This study employed a two fluid atomizer for spray depositing the materials in the form of precursor inks. Compared to the ultrasonic and electrostatic atomizers, the two fluid atomizers are capable of atomizing liquids within a wide range of rheological properties and deliver high flow rates [34,43], and are less prone to clogging of the nozzle due to the large passages [44].

This study required printing of up to two layers of the EAP and three layers of the electrodes (dual-layer design), but the same methods can also be used to print more alternating layers to produce multi-layer stack transducers. While only two different functional materials were needed to produce the actuators, additional materials can be introduced to spray-print also the structural materials (e.g. the substrate or mechanisms). The precursor materials need to be in the liquid form, and require post-processing for curing or evaporating the solvents. Other limitations in spray printing include non-uniform deposition profile, irregular boundaries, satellite droplets and limited x-y resolution. Proceeding from the 2.5D structures to the true 3D printing requires introduction of support materials, similar to the IJP [45]. Since the spray printing resolution is strongly anisotropic (0.5 mm in x-y and 0.63 μm in thickness direction), 3D printing using only the airbrush tools limits the printable geometries. Alternatively, spray printing can be combined with other 3D printing methods such as extrusion printing, allowing to create more complex structures and devices (e.g. mechanisms, sensors, actuators, electronics).

Versatility of the system was demonstrated by fabricating P(VDF-TrFE-CTFE) actuators that exceeded the performance of the previously reported similar actuators. While the actuator fabrication involved two manual steps (i.e. drying steps and changing between inks), full automation is possible by adding the second airbrush and implementing the drying routines within the printer and the GCODE. At the components costing a total of <€1000, the airbrush 3D printer costs a fraction of the IJP or AJP systems. The proposed printing method is anticipated to significantly facilitate the manufacturing of both the electronic and ionic EAP actuators, and many other stimuli-responsive device.

4.2. EAP ink formulation

While the electrodes of the actuators were printed from a commercially available ink, the P(VDF-TrFE-CTFE) ink had to be formulated in-house. The best combination of rheological- and drying properties was attained at the MEK 90:10 DMSO solvent mixture and 7%wt P(VDF-TrFE-CTFE) loading factor, i.e. at a 6 times higher concentration than is feasible to jet in inkjet printing [30]. The higher DMSO concentrations left a noticeable solvent residue on the EAP film after the deposition (while the MEK evaporation is almost immediate), causing the ink to smear and significantly increasing the drying time. The DMSO concentrations below 10%wt caused an unreliable printing process due to the frequent airbrush clogging. For the 90:10 mixture the clogging intervals increased significantly, and were completely prevented by executing occasional purging routines. The P(VDF-TrFE-CTFE) loading factors below 7%wt increased the EAP ink drying time, while the higher loading factors caused inconsistent spraying.

4.3. Deposition settings

Developing the high-resolution printing recipes attained a reliable deposition at the narrowest line widths of 0.5 mm. Smaller feature sizes were observable in some of the samples, but their implementation was limited by the clogging and inconsistent deposition. Variations in the line widths and the satellite droplet formation confirm that the atomizing regime is significantly affected by the ink valve position and the air supply pressure. The rate of material deposition is limited by the spreading of the deposited material, observable at small nozzle-substrate offsets and at low printing speeds. This becomes more pronounced in the beginning and end of the lines, where the speed of motion is not continuous. Substrate-needle offsets below 0.5 mm were not studied due to the elevated risk of the airbrush-sample collision.

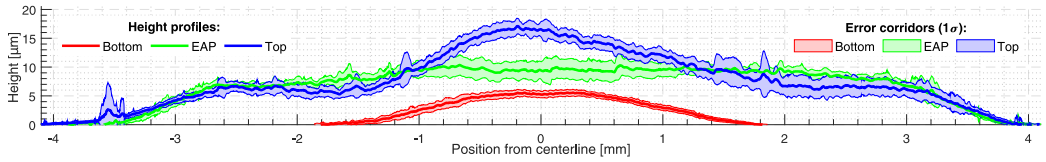

Fig. 14. Average height profiles after depositing (A) the bottom electrode, (B) the P(VDF-TrFE-CTFE) layer and (C) the top electrode. These profiles correspond to the topology graphs in Fig. 13.

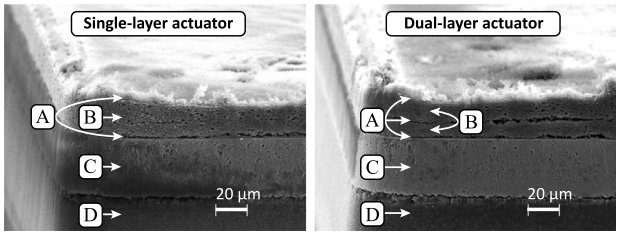

Fig. 15. SEM images of the actuator cross-sections. The visible components are indicated as: A – the electrodes; B – the EAP layers; C – the microporous resin portion of the substrate; and D – the PET substrate.

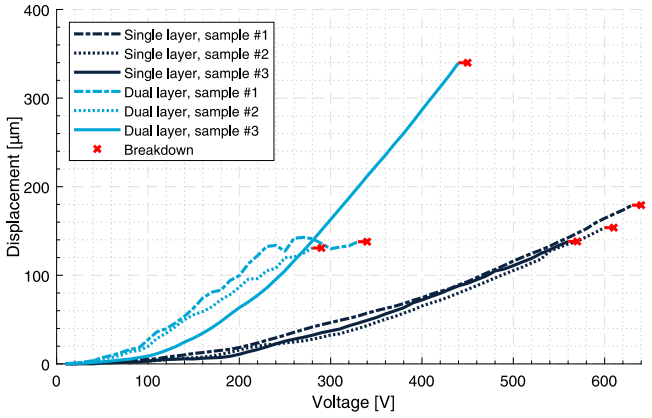

Fig. 16. Voltage-deflection behavior and breakdown voltages of the single- and dual-layer actuators.

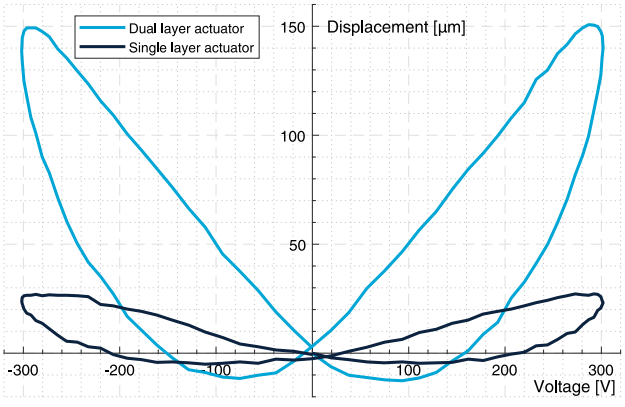

Fig. 17. Hysteresis behavior of the single- and dual-layer actuators in response to 1 Hz sinusoidal excitation.

4.4. Printing functional inks

Spray printing proved as a robust method for printing inks in a wide range of rheological properties and suspended particles sizes. Spray printing the P(VDF-TrFE-CTFE) inks at a 7%wt EAP content is a 460% higher concentration than the 1.25%wt maximum reported in IJP [30].

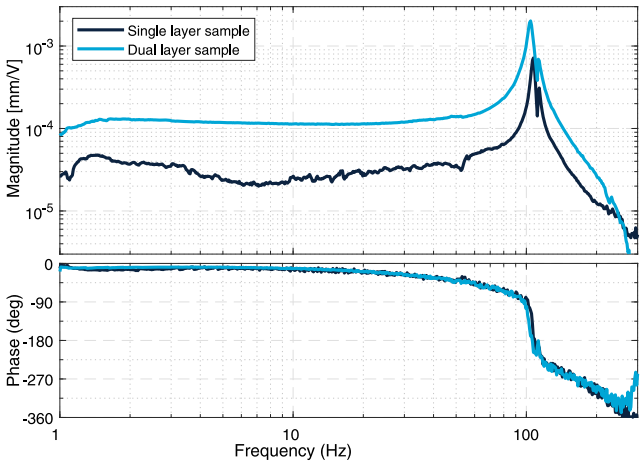

Fig. 18. Frequency responses of the single- and dual-layer actuators upon 100 V_{pp} excitation.

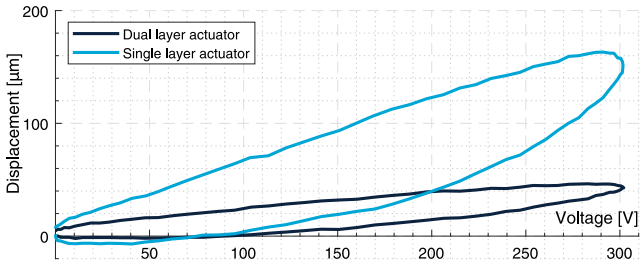

Fig. 19. Actuation hysteresis upon unipolar excitation (1 Hz).

Consistent printing of the carbon black ink allowed to develop a reliable deposition process, in contrast to the more problematic IJP process that is susceptible to nozzle clogging and eventual printhead failures [29,30,36]. While the ink specifications report a z-average particle size of 120 nm to 150 nm [37], the distribution includes much bigger particles (spread is not specified), and a further agglomeration occurs over time. In fact, the ink could not be filtered through 0.45 µm filters, and 5 µm filters had to be used. For reliable printing the nozzle diameters must be ≥ 50x larger than the particles in the ink [26], making most of the IJP nozzles much smaller than ideal (e.g. 20 µm in a Dimatix DMC-11610). Spray printing circumvents this challenge since the atomizer orifice size is directly controllable via the ink valve position.

The porosity of the substrate and the bottom electrode (i.e. carbon black) functioned well in constraining the motion of the inks after printing, reducing the spreading and preventing the coffee ring effect. While the first steps of top electrode deposition produced a visibly non-uniform electrode layer on top of the smooth EAP surface, alternating the printing with drying in four steps made this non-uniformity to gradually disappear. It is hypothesized that the build-up of the carbon black particles posed a restriction to the ink flow.

4.5. Resolution

The results of this study showed sub-mm in-plane resolutions and sub-μm thickness resolutions. While the robustness and simplicity of spray printing comes with the penalty of reduced in-plane resolution, this is well acceptable in most smart material use cases. High deposition quality in thickness direction on the other hand is essential for the high breakdown field strengths, allowing to form strong electric fields within the EAP, and produce high strains.

Spray printing resolution can be altered via the printing settings, allowing to deposit finer features at a limited speed, and a faster coverage of larger areas at a lower resolution, using the same system. Compared to the IJP, the EAP deposition time was reduced by ca 16x, from ca 8 h [30] down to 14 min. A single actuator fabrication takes 3 h, constituting of a 30 min printing time, 30 min drying time and 2 h curing time. Simultaneously achieving high deposition rates and fine resolutions however is limited by a trade-off between these parameters.

The finest line widths that were reliably printed in this study were 0.5 mm. This is inferior to the < 100 μm lines attainable by IJP [46], the 10 μm lines possible in AJW [47] and the 0.18 mm nozzle diameter of the airbrush [35]. Deposition of finer lines is anticipated to be possible by using less volatile solvents, optimizing the printing recipes, or adapting more complicated atomizer designs that apply sheath gas for aerodynamic focusing, similar to the AJP [47].

EAP deposition thickness resolution was calculated to be 0.63 μm for the 0.7 mm in-plane resolution (since the 2 × 16 repetitions yield a 20 μm layer thickness). It is hypothesized that the high layer resolution and quality (i.e. uniform film thickness and lack of pinhole defects) were the key reason for the significant performance improvement over the past reports [29,30]. Since the film thickness depends both on the printing settings and the functional material loading factor in the ink, it is possible to further improve this resolution.

4.6. Actuators

Airbrush 3D printing allowed fast and repeatable deposition of the carbon black and P(VDF-TrFE-CTFE) inks. For these materials the intermediate fabrication steps are limited to drying and heating, avoiding the need for more elaborate processes and equipment, such as plasma treatment or photonic curing [36]. While the drying and curing are time-consuming steps, they are low on human labor and feasible to automate. Using solvent annealing process in place of thermal annealing can improve the actuation performance and avoid the need for curing at high temperatures, while further increasing the total fabrication time [48].

A high dielectric breakdown strength is an indicator of a good quality of the EAP layer. All the single layer samples operated reliably at up to 550 V and one of the dual layer samples at up to 440 V. Breakdown field strength for the single layer (20 μm EAP) samples was estimated to be > 27.5 V/μm, which is consistent with the literature [29,30]. For one of the dual layer (2x 10 μm EAP) samples the > 44.0 V/μm breakdown field strength exceeds the prior reports. While the other two dual layer samples failing above 280 V and 330 V is consistent with the breakdown field strengths of the single-layer samples, the significantly lower through-actuator resistances (< 100 kΩ versus ca 40 MΩ of the third actuator) indicate the presence of imperfections in their EAP layers. Breakdown strength of the pure EAP material is specified by the manufacturer at > 350 V/μm [40]. The much lower breakdown is hypothesized to be caused by the surface roughness of the bottom electrode (carbon black), contaminants within the EAP, and undesired porosity caused by the solvent evaporation dynamics [49,50]. Therefore, reviewing the electrode material choice and further optimization of the fabrication process is anticipated to improve the actuation performance.

The voltage-displacement behavior of all the actuators was consistent with the relaxor ferroelectric EAPs [51], exhibiting hysteresis in the actuation and displaying a quadratic relation between the electric field and the material strain. The quadratic relation also exhibits in the ca 4x higher strains per volt of the dual-layer samples over the single-layer ones, caused by the EAP layers being ca 2x thinner. Using two EAP layers of half the thickness allows to produce the same electric field strength within the EAP at half the input voltage (total thickness is the same, opposite polarization in adjacent layers). This is desirable to lower the actuation voltages while not affecting the actuation capabilities. The actuation hysteresis (see Figs. 17 and 19) indicates a significant energy dissipation due to the viscoelastic behavior of the actuator components (most probably dominated by the microporous coating of the IJ-220 substrate) and partially also due to the cyclic alteration of the EAP polarization [40].

Previously reported similar P(VDF-TrFE-CTFE) actuators produced up to 224 μm (275 V) quasi-static displacements [30] and 3 mm (300 V) resonant displacements [29]. In comparison (see Table 3), the dual-layer actuators showed 51% higher quasi-static deflections (i.e. 340 μm, 440 V_{pp}) and 24% higher resonant deflections (i.e. 3.7 mm, 400 V_{pp}, 104 Hz). While the single-layer samples performed inferior to the dual-layer ones, the performance difference compared to the prior art remains below 21% in the quasi-static (179 μm, 630 V_{pp}) and 34% in resonant operation (2.0 mm, 600 V_{pp}, 107 Hz). Frequency responses (Fig. 18) and resonant frequencies remained in the 100 Hz to 110 Hz interval, being consistent with the past reports (Table 3).

Performance (force, stroke) and stiffness of the unimorph bending actuators have been shown to be a trade-off between the thicknesses and elastic moduli of their constituent materials [52,53]. Optimization of these parameters was not addressed in this study, and actuator morphology can further be tailored to maximize the attainable displacements or forces, or to target more specific mechanical impedance (i.e. force–displacement) objectives.

5. Conclusion

This paper proposed an airbrush-based 3D printer for additive manufacturing of smart material transducers. An airbrush 3D printer was built, a process was developed for fabricating relaxor ferroelectric actuators, and the performance of the resulting actuators was studied.

Spray printing was demonstrated to enable contact-less, mask-less and automated deposition of functional inks in custom design patterns. It enabled printing inks in a wide range of rheological properties and suspended particle sizes. Printing recipe development attained fast and repeatable deposition of EAP and carbon black inks at a 0.5 mm in-plane resolution and a 0.63 μm thickness resolution. The system is simple to construct and operate, and its cost is comparable to the entry level 3D printers.

Versatility of the system was demonstrated by fabricating P(VDF-TrFE-CTFE) actuators, showing a significant performance improvement over previously reported similar actuators. Bending cantilever actuators with a single and dual active layers were printed at 0.7 mm in-plane resolution. The actuator electrodes based on a commercial carbon black ink and the EAP layer based on a custom-formulated P(VDF-TrFE-CTFE) ink. Spray printing allowed to deposit inks with up to 7% EAP content, attaining a 460% higher loading factor and a 16x faster EAP print time compared to the inkjet printing process. The single-layer actuators attained 179 μm quasi-static and 2 mm resonant displacements (107 Hz). The dual layer actuators showed 340 μm quasi-static and 3.7 mm resonant displacements (104 Hz). Compared to the previously reported similar actuators, this means a 51% and a 24% improvement, respectively.

Spray printing with a fine airbrush allows to print materials that are problematic to handle in other 3D printing techniques. It allows to create complex geometries at sub-mm in-plane resolution and sub-μm thickness resolution. The proposed printing method is anticipated to significantly facilitate the manufacturing and development of both the electronic and ionic EAP actuators, and many other stimuli-responsive device.

CRediT authorship contribution statement

Stijn IJssel de Schepper: Writing – original draft, Visualization, Validation, Software, Project administration, Methodology, Investigation, Formal analysis, Data curation. **Andres Hunt:** Writing – review & editing, Visualization, Supervision, Resources, Project administration, Methodology, Investigation, Funding acquisition, Conceptualization.

Declaration of competing interest

The authors declare that they have no known competing financial interests or personal relationships that could have appeared to influence the work reported in this paper.

Data availability

Data will be made available on request.

Appendix A. Supplementary data

Supplementary material related to this article can be found online at https://doi.org/10.1016/j.addma.2024.103982.

References

[1] Y. Bar-Cohen, Q. Zhang, Electroactive polymer actuators and sensors, MRS Bull. 33 (3) (2008) 173–181, http://dx.doi.org/10.1557/mrs2008.42.

[2] Y. Bar-Cohen, Electroactive polymers as an enabling materials technology, Proc. Inst. Mech. Eng. G-J. Aerosp. Eng. 221 (4) (2007) 553–564, http://dx.doi.org/10.1243/09544100JAERO141.

[3] S.J. Rupitsch, Piezoelectric sensors and actuators, in: Topics in Mining, Metallurgy and Materials Engineering, 2019, http://dx.doi.org/10.1007/978-3-662-57534-5.

[4] F. Soto, E. Karshalev, F. Zhang, B. Esteban Fernandez de Avila, A. Nourhani, J. Wang, Smart materials for microrobots, Chem. Rev. 122 (5) (2022) 5365–5403, http://dx.doi.org/10.1021/acs.chemrev.0c00999.

[5] V. Giurgiutiu, Review of smart-materials actuation solutions for aeroelastic and vibration control, J. Intell. Mater. Syst. Struct. 11 (7) (2000) 525–544, http://dx.doi.org/10.1106/HYTV-NC7R-BCMM-W3CH.

[6] P. Motreuil-Ragot, A. Hunt, D. Kasi, B. Brajon, A.v.d. Maagdenberg, V. Orlova, M. Mastrangeli, P.M. Sarro, Enabling actuation and sensing in organs-on-chip using electroactive polymers, in: 2020 3rd IEEE International Conference on Soft Robotics, RoboSoft, 2020, pp. 530–535, http://dx.doi.org/10.1109/RoboSoft48309.2020.9115977.

[7] E.A. Sideris, H.C. de Lange, A. Hunt, An Ionic Polymer Metal Composite (IPMC)-Driven linear peristaltic microfluidic pump, IEEE Robot. Autom. Lett. 5 (4) (2020) 6788–6795, http://dx.doi.org/10.1109/LRA.2020.3015452.

[8] M.Q. Le, J.-F. Capsal, J. Galineau, F. Ganet, X. Yin, M. Yang, J.-F. Chateaux, L. Renaud, C. Malhaire, P.-J. Cottinet, R. Liang, All-organic electrostrictive polymer composites with low driving electrical voltages for micro-fluidic pump applications, Sci. Rep. 5 (1) (2015) 11814, http://dx.doi.org/10.1038/srep11814.

[9] S.D. Mahapatra, P.C. Mohapatra, A.I. Aria, G. Christie, Y.K. Mishra, S. Hofmann, V.K. Thakur, Piezoelectric materials for energy harvesting and sensing applications: Roadmap for future smart materials, Adv. Sci. 8 (17) (2021) 2100864, http://dx.doi.org/10.1002/advs.202100864.

[10] X. Qiu, G.C. Schmidt, P.M. Panicker, R.A. Quintana Soler, A.J. Benjamin, A.C. Hübler, Fully printed piezoelectric polymer loudspeakers with enhanced acoustic performance, Adv. Eng. Mater. 21 (11) (2019) 1900537, http://dx.doi.org/10.1002/adem.201900537.

[11] B. Kim, B.M. Kim, J. Ryu, I.-H. Oh, S.-K. Lee, S.-E. Cha, J. Pak, Analysis of mechanical characteristics of the ionic polymer metal composite (IPMC) actuator using cast ion-exchange film, in: Y. Bar-Cohen (Ed.), Smart Structures and Materials 2003: Electroactive Polymer Actuators and Devices, Vol. 5051, EAPAD, SPIE, International Society for Optics and Photonics, 2003, pp. 486–495, http://dx.doi.org/10.1117/12.484296.

[12] V.F. Cardoso, C.M. Costa, G. Minas, S. Lanceros-Mendez, Improving the optical and electroactive response of poly(vinylidene fluoride–trifluoroethylene) spin-coated films for sensor and actuator applications, Smart Mater. Struct. 21 (8) (2012) 085020, http://dx.doi.org/10.1088/0964-1726/21/8/085020.

[13] T.H.T. Fook, J.H. Jeon, P.S. Lee, Transparent flexible polymer actuator with enhanced output force enabled by conductive nanowires interlayer, Adv. Mater. Technol. 5 (1) (2020) 1900762, http://dx.doi.org/10.1002/admt.201900762.

[14] S. Ahmed, Z. Ounaies, E.A.F. Arrojado, Electric field-induced bending and folding of polymer sheets, Sensors Actuators A 260 (2017) 68–80, http://dx.doi.org/10.1016/j.sna.2017.03.025.

[15] O. Araromi, A. Conn, C. Ling, J. Rossiter, R. Vaidyanathan, S. Burgess, Spray deposited multilayered dielectric elastomer actuators, Sensors Actuators A 167 (2) (2011) 459–467, http://dx.doi.org/10.1016/j.sna.2011.03.004.

[16] W. Yuan, L. Hu, S. Ha, T. Lam, G. Grüner, Q. Pei, Self-clearable carbon nanotube electrodes for improved performance of dielectric elastomer actuators, in: Y. Bar-Cohen (Ed.), Electroactive Polymer Actuators and Devices (EAPAD) 2008, San Diego, California, 2008, p. 69270P, http://dx.doi.org/10.1117/12.776809.

[17] Schmidt, Lediaev, Polasik, Hallenberg, Piezoelectric actuators employing PVDF coated with flexible PEDOT-PSS polymer electrodes, IEEE Trans. Dielectrics Electr. Insul. 13 (5) (2006) 1140–1148, http://dx.doi.org/10.1109/TDEI.2006.247842.

[18] Z. Peng, Y. Shi, N. Chen, Y. Li, Q. Pei, Stable and high-strain dielectric elastomer actuators based on a carbon nanotube-polymer bilayer electrode, Adv. Funct. Mater. 31 (9) (2021) 2008321, http://dx.doi.org/10.1002/adfm.202008321.

[19] J.D. Carrico, N.W. Traeden, M. Aureli, K.K. Leang, Fused filament 3D printing of ionic polymer-metal composites (IPMCs), Smart Mater. Struct. 24 (12) (2015) 125021, http://dx.doi.org/10.1088/0964-1726/24/12/125021.

[20] G. Yin, Q. He, X. Zhou, Y. Wu, H. Li, M. Yu, Printing ionic polymer metal composite actuators by fused deposition modeling technology, Int. J. Smart Nano Mater. 12 (2) (2021) 218–231, http://dx.doi.org/10.1080/19475411.2021.1914766.

[21] H. Pei, J. Jing, Y. Chen, J. Guo, N. Chen, 3D printing of PVDF-based piezoelectric nanogenerator from programmable metamaterial design: Promising strategy for flexible electronic skin, Nano Energy 109 (2023) 108303, http://dx.doi.org/10.1016/j.nanoen.2023.108303.

[22] A. Chortos, E. Hajiesmaili, J. Morales, D.R. Clarke, J.A. Lewis, 3D printing of interdigitated dielectric elastomer actuators, Adv. Funct. Mater. 30 (1) (2020) 1907375, http://dx.doi.org/10.1002/adfm.201907375.

[23] A. Chortos, J. Mao, J. Mueller, E. Hajiesmaili, J.A. Lewis, D.R. Clarke, Printing reconfigurable bundles of dielectric elastomer fibers, Adv. Funct. Mater. 31 (22) (2021) 2010643, http://dx.doi.org/10.1002/adfm.202010643.

[24] R.S. Pinto, J.P. Serra, J.C. Barbosa, R. Gonçalves, M.M. Silva, S. Lanceros-Méndez, C.M. Costa, Direct-ink-writing of electroactive polymers for sensing and energy storage applications, Macromol. Mater. Eng. 306 (11) (2021) 2100372, http://dx.doi.org/10.1002/mame.202100372.

[25] B. García-Farrera, L.F. Velásquez-García, Ultrathin ceramic piezoelectric films via room-temperature electrospray deposition of ZnO nanoparticles for printed GHz devices, ACS Appl. Mater. Interfaces 11 (32) (2019) 29167–29176, http://dx.doi.org/10.1021/acsami.9b09563.

[26] I.M. Hutchings, G. Martin (Eds.), Inkjet Technology for Digital Fabrication, Wiley, Chichester, West Sussex, United Kingdom, 2013, http://dx.doi.org/10.1002/9781118452943.

[27] S. Reitelshöfer, M. Göttler, P. Schmidt, P. Treffer, M. Landgraf, J. Franke, Aerosol-Jet-Printing silicone layers and electrodes for stacked dielectric elastomer actuators in one processing device, in: Y. Bar-Cohen, F. Vidal (Eds.), Electroactive Polymer Actuators and Devices (EAPAD) 2016, 9798, SPIE, International Society for Optics and Photonics, Las Vegas, Nevada, United States, 2016, p. 97981Y, http://dx.doi.org/10.1117/12.2219226.

[28] Y. Zhang, C. Liu, D. Whalley, Direct-write techniques for maskless production of microelectronics: A review of current state-of-the-art technologies, in: 2009 International Conference on Electronic Packaging Technology & High Density Packaging, IEEE, Beijing, China, 2009, pp. 497–503, http://dx.doi.org/10.1109/ICEPT.2009.5270702.

[29] K.K. Baelz, A. Hunt, P(VDF-TrFE-CTFE) actuators with inkjet printed electrodes, in: 2019 7th International Conference on Control, Mechatronics and Automation, ICCMA, IEEE, Delft, Netherlands, 2019, pp. 327–332, http://dx.doi.org/10.1109/ICCMA46720.2019.8988745.

[30] S.A. Sekar, Manufacturing Process for Inkjet-Printing a Relaxor Ferroelectric Actuator, Delft University of Technology, Delft, the Netherlands, 2021, URL https://repository.tudelft.nl/islandora/object/uuid:173c1687-e31a-45aa-9750-700d0036a561.

[31] E. Tekin, P.J. Smith, U.S. Schubert, Inkjet printing as a deposition and patterning tool for polymers and inorganic particles, Soft Matter 4 (2008) 703–713, http://dx.doi.org/10.1039/b711984d.

[32] R.I. Haque, R. Vié, M. Germainy, L. Valbin, P. Benaben, X. Boddaert, Inkjet printing of high molecular weight PVDF-TrFE for flexible electronics, Flexible Printed Electron. 1 (1) (2015) 015001, http://dx.doi.org/10.1088/2058-8585/1/1/015001.

[33] S. Reitelshofer, M. Landgraf, D. Graf, L. Bugert, J. Franke, A new production process for soft actuators and sensors based on dielectric elastomers intended for safe human robot interaction, in: 2015 IEEE/SICE International Symposium on System Integration, SII, IEEE, Nagoya, 2015, pp. 51–56, http://dx.doi.org/10.1109/SII.2015.7404953.

[34] A.H. Lefebvre, V.G. McDonell, Atomization and Sprays (2nd ed.), CRC Press, Boca Raton, 2017, http://dx.doi.org/10.1201/9781315120911.

[35] Iwata custom micron takumi side feed dual action airbrush, Anest Iwata-Medea, Inc., URL https://www.iwata-airbrush.com/iwata-custom-micron-takumi-side-feed.html.

[36] K.K. Baelz, A. Hunt, Printing electrodes for P(VDF-TrFE-CTFE) actuators using a consumer-grade inkjet printer, in: H.R. Shea, I.A. Anderson, J.D.W. Madden (Eds.), Electroactive Polymer Actuators and Devices (EAPAD) XXV, Vol. 12482, SPIE, International Society for Optics and Photonics, 2023, p. 124820P, http://dx.doi.org/10.1117/12.2660469.

[37] NovaCentrix, JR-700HV Carbon Black Nanoparticle Ink, 2023, Online: https://www.novacentrix.com/product/jr-700hv-carbon-black-nanoparticles/. (Accessed: 8 July 2023).

[38] Metalon® JS-A221AE Silver ink, 2012, NCC Nano LLC dba NovaCentrix, URL https://www.novacentrix.com/datasheet/Metalon-JS-A221AE-SDS.pdf, NCC Nano LLC dba NovaCentrix: 400 Parker Drive, Suite 1110, Austin, TX 78728.

[39] Metalon® CI-004 Copper ink, 2012, NCC Nano LLC dba NovaCentrix, URL https://www.novacentrix.com/datasheet/Metalon-CI-004-SDS.pdf, NCC Nano LLC dba NovaCentrix: 400 Parker Drive, Suite 1110, Austin, TX 78728.

[40] Piezotech RT-TS, 2020, Piezotech Arkema CRRA, URL https://page.arkema.com/rs/253-HSZ-754/images/Technical%20Guide%20Piezotech%20RT-TS.pdf, Piezotech Arkema CRRA: Rue Henri Moissan, 69496 Pierre-Benite Cedex, France.

[41] P.-H. Ducrot, I. Dufour, C. Ayela, Optimization of PVDF-TrFE processing conditions for the fabrication of organic MEMS resonators, Sci. Rep. 6 (1) (2016) 19426, https://doi.org/10.1038/srep19426.

[42] F. Bauer, Relaxor fluorinated polymers: Novel applications and recent developments, IEEE Trans. Dielectr. Electr. Insul. 17 (4) (2010) 1106–1112, http://dx.doi.org/10.1109/TDEI.2010.5539681.

[43] G.G. Nasr, A.J. Yule, L. Bendig, Industrial Sprays and Atomization: Design, Analysis and Applications, Springer London, 2002, http://dx.doi.org/10.1007/978-1-4471-3816-7.

[44] H. Liu, 2.1.1 Pressure Jet Atomization, in: Science and Engineering of Droplets - Fundamentals and Applications, William Andrew Publishing Noyes, 2000, URL https://www.sciencedirect.com/science/book/9780815514367.

[45] Stratasys, Polyjet technology for 3D printing, 2023, Guide to 3D printing, Stratasys Direct, Inc., URL https://www.stratasys.com/en/guide-to-3d-printing/technologies-and-materials/polyjet-technology/. (Accessed: 20 December 2023).

[46] D. Soltman, V. Subramanian, Inkjet-printed line morphologies and temperature control of the coffee ring effect, Langmuir 24 (5) (2008) 2224–2231, http://dx.doi.org/10.1021/la7026847.

[47] E. Jabari, E. Toyserkani, Micro-scale aerosol-jet printing of graphene interconnects, Carbon 91 (2015) 321–329, http://dx.doi.org/10.1016/j.carbon.2015.04.094.

[48] Y. Cho, D. Ahn, J.B. Park, S. Pak, S. Lee, B.O. Jun, J. Hong, S.Y. Lee, J.E. Jang, J. Hong, S.M. Morris, J.I. Sohn, S.N. Cha, J.M. Kim, Enhanced ferroelectric property of P(VDF-TrFE-CTFE) film using room-temperature crystallization for high-performance ferroelectric device applications, Adv. Electron. Mater. 2 (10) (2016) 1600225, http://dx.doi.org/10.1002/aelm.201600225.

[49] G.R. Guillen, Y. Pan, M. Li, E.M. Hoek, Preparation and characterization of membranes formed by nonsolvent induced phase separation: A review, Ind. Eng. Chem. Res. 50 (7) (2011) 3798–3817, http://dx.doi.org/10.1021/ie101928r.

[50] H. Matsuyama, H. Karkhanechi, S. Rajabzadeh, Chapter 3 - polymeric membrane fabrication via thermally induced phase separation (TIPS) method, in: T.-S. Chung, Y. Feng (Eds.), Hollow Fiber Membranes, Elsevier, 2021, pp. 57–83, http://dx.doi.org/10.1016/B978-0-12-821876-1.00021-4.

[51] N. Della Schiava, K. Thetpraphi, M.-Q. Le, P. Lermusiaux, A. Millon, J.-F. Capsal, P.-J. Cottinet, Enhanced figures of merit for a high-performing actuator in electrostrictive materials, Polymers 10 (3) (2018) 263, http://dx.doi.org/10.3390/polym10030263.

[52] M.R.A. Nabawy, B. Parslew, W.J. Crowther, Dynamic performance of unimorph piezoelectric bending actuators, Proc. Insti. Mech. Eng. I 229 (2) (2015) 118–129, http://dx.doi.org/10.1177/0959651814552810.

[53] Q.-M. Wang, L.E. Cross, Tip deflection and blocking force of soft PZT-based cantilever RAINBOW actuators, J. Am. Ceram. Soc. 82 (1) (1999) 103–110, http://dx.doi.org/10.1111/j.1151-2916.1999.tb01729.x.